

THE COLLAPSE OF EXOTIC TEXTURESAndrew Sornborger,⁽¹⁾ Sean M. Carroll,⁽²⁾ and Ted Pyne⁽³⁾

⁽¹⁾*Department of Applied Mathematics and Theoretical Physics
University of Cambridge
Silver Street, Cambridge CB3 9EW
Great Britain*

email: A.T.Sornborger@damtp.cam.ac.uk

⁽²⁾*Institute for Theoretical Physics
University of California
Santa Barbara, California 93106
email: carroll@itp.ucsb.edu*

⁽³⁾*Harvard-Smithsonian Center for Astrophysics
Cambridge, Massachusetts 02138
email: pyne@cfa160.harvard.edu*

Abstract

The ordering of scalar fields after a phase transition in which a group G of global symmetries is spontaneously broken to a subgroup H provides a possible explanation for the origin of structure in the universe, as well as leading to observable effects in condensed matter systems. The field dynamics can depend in principle on the geometry and topology of the vacuum manifold G/H ; for example, texture configurations which collapse and unwind will exist if the third homotopy group $\pi_3(G/H)$ is nontrivial. We numerically simulate the evolution of texture-like configurations in a number of different models, in order to determine the extent to which the geometry and topology of the vacuum manifold influences the field evolution. We find that the dynamics is affected by whether or not the theory supports strings or monopoles [characterized by $\pi_1(G/H)$ and $\pi_2(G/H)$, respectively]. In some of the theories studied, configurations with initially spherically symmetric energy densities are unstable to nonspherical collapse; these theories are also found to nucleate defects during the collapse. Models that do not support monopoles or strings behave similarly to each other, regardless of the specific vacuum manifold.

I. Introduction

Our understanding of large-scale inhomogeneities in the universe, both directly through surveys of the distances and velocities of galaxies and indirectly through observations of temperature fluctuations in the cosmic microwave background, has advanced significantly in recent years. This growth in empirical knowledge has necessitated greater precision in the extraction of predictions from theoretical models; claiming that a theory is consistent with observation requires more care now than it did a decade ago. As a result, it has become important to pay close attention to the differences between various manifestations of any general scenario. This paper takes up this task for the texture model of structure formation, and studies the extent to which the geometry and topology of the vacuum manifold in a scalar field theory can exert a cosmologically significant influence on the dynamics of the fields. Although our discussion is phrased in terms of cosmological effects, analogous considerations hold for condensed matter systems with spontaneously broken global symmetries.

In the texture scenario, we consider a set of scalar fields Φ which transform under a global symmetry group G . If the potential $V(\Phi)$ is such that this symmetry is spontaneously broken to a subgroup H , the potential will possess a set of degenerate minima. This set of field values is known as the vacuum manifold \mathcal{M} , and is isomorphic to the quotient space G/H . Typically, at high temperatures the expectation value of the field is the same everywhere; as the universe cools the fields will relax to the vacuum manifold, and according to the Kibble mechanism the points to which the field evolves will be uncorrelated on distances greater than the Hubble distance at that epoch. The fields will tend to order themselves, approaching a constant-field configuration within a causally connected region, but as the Hubble distance grows the fields will always be uncorrelated on cosmological scales. The resulting gradient energy leads to an approximately scale-free spectrum of energy density perturbations, which can serve as seeds for large-scale structure.

Depending on the topology of the vacuum manifold, the scalar fields may be forced to leave \mathcal{M} in order to smooth themselves out. This can be seen by considering a configuration which is confined to \mathcal{M} , and is set to some fixed value outside a certain radius. This is mathematically equivalent to compactifying three-dimensional space to a three-sphere, and the resulting field configuration defines a map $S^3 \rightarrow \mathcal{M}$. Such maps are classified topologically by the third homotopy group $\pi_3(\mathcal{M})$; if the configuration corresponds to a nontrivial element of $\pi_3(\mathcal{M})$, then it cannot be smoothly deformed to a constant-field configuration. In this case, it is energetically favorable for the configuration to shrink in size until the energy density reaches that needed to leave the vacuum manifold. The field then “unwinds” by climbing over the energy barrier to a topologically trivial configuration. Turok [1] suggested that this process of collapse and unwinding could lead to seeds for the formation of large-scale structure. It was later realized [2,3] that scalar field gradients could lead to density perturbations even if $\pi_3(\mathcal{M})$ were trivial.

Even though density perturbations will be produced for any theory with spontaneously broken exact global symmetries, it is reasonable to imagine that the detailed dynamics of the fields (and hence the specific prediction for perturbations) will depend on the topology of the vacuum manifold. Indeed, two different models with nontrivial $\pi_3(\mathcal{M})$, which support texture configurations with nonzero winding, may nevertheless predict different evolutions for the collapsing texture, and such differences may manifest themselves cosmologically. At the same time, it may be possible for configurations which are topologically trivial to evolve in ways similar to what we would call a texture.

In this paper we explore some of these issues. We consider theories of scalar fields transforming under global symmetry groups; the theories are specified by the group G , the representation of G under which the fields Φ transform, and the potential energy $V(\Phi)$. Li [4] has considered a number of such theories, and determined what the unbroken symmetry group H will be in each model. Bryan, Carroll and Pyne [5] have examined the topology of

the resulting vacuum manifolds $\mathcal{M} = G/H$, and calculated the homotopy groups $\pi_1(\mathcal{M})$, $\pi_2(\mathcal{M})$, and $\pi_3(\mathcal{M})$. (Just as $\pi_3(\mathcal{M})$ characterizes textures, $\pi_1(\mathcal{M})$ characterizes cosmic strings and $\pi_2(\mathcal{M})$ characterizes monopoles.) Here we have chosen eight different models, listed in Table One, which represent a variety of different field contents and vacuum manifold topologies.

To understand in full detail the cosmological effects of each of these theories, it would be necessary to do a number of full-scale numerical simulations of large-scale structure formation or CMB anisotropy in each model, such as those which have been performed for the models with $\mathcal{M} = S^3$ [6,3]. We have adopted a more modest approach, since our goal is simply to determine whether the choice of vacuum manifold exerts an influence over the dynamics. Our strategy is therefore to set up comparable field configurations in the various theories, each corresponding to a single texture. We then follow numerically the evolution of the configurations as they collapse and evaporate away, keeping track of the distribution of energy into potential, kinetic and gradient energy, as well as the asymmetry of the collapse as measured by the quadrupole moments of the total energy density. (For analogous studies of the usual texture models, see [7,8].) In each model we performed three simulations: one in which the energy density was initially spherically symmetric, one which was initially prolate (cigar-shaped), and one which was initially oblate (pancake-shaped).

As detailed below, we find that the models studied fall naturally into two different categories of behavior. Within each of the two classes, the evolution of the energy densities and quadrupole moments is relatively similar for each type of collapse, while there is a noticeable difference between the two categories. In the eight models we studied, the division corresponds precisely to whether the theory supports strings or monopoles; *i.e.*, to whether or not $\pi_1(\mathcal{M})$ and $\pi_2(\mathcal{M})$ are trivial. All of the models without these defects evolved in one way, while those which do support defects evolved in a distinct fashion. Upon examination of the simulations, we discover that in some of the models defects are

nucleated in the process of collapse; however this is not always true, and is therefore not a sufficient explanation for the division into two types of collapse.

II. Initial Configurations

The models we consider are described by Lagrangians of the form

$$\mathcal{L} = \frac{1}{2} \partial_\mu \Phi \cdot \partial^\mu \Phi - V(\Phi) . \quad (2.1)$$

Here, Φ stands for a collection of N scalar fields which transform under some representation of a global symmetry group G . The product $\Phi_1 \cdot \Phi_2$ is the invariant inner product appropriate to the representation; for a vector Φ^a we have $\Phi_1 \cdot \Phi_2 = \sum_a \Phi_1^{a*} \Phi_2^a$ (where an asterix denotes complex conjugation), while for a matrix Φ^{ab} we have $\Phi_1 \cdot \Phi_2 = \sum_{ab} \Phi_1^{ab*} \Phi_2^{ab} = \text{Tr}(\Phi_1^\dagger \Phi_2)$. The potential $V(\Phi)$ consists of terms quadratic and quartic in the fields.

We are interested in constructing, for each theory, initial field configurations which are wholly in the vacuum manifold and which have unit winding number. We follow the procedure outlined in [5]. The basis of this procedure is the fact that every field value in the vacuum manifold may be obtained by starting with a fixed vacuum expectation value $\langle \Phi \rangle$ and acting on it by an element of the symmetry group G . The initial configuration can therefore be written

$$\Phi(\mathbf{x}) = \mu(\mathbf{x}) \langle \Phi \rangle , \quad (2.2)$$

where $\mu(\mathbf{x})$ is a position-dependent element of G . (The notation $\mu(\mathbf{x}) \langle \Phi \rangle$ indicates the action of μ on the representation carried by $\langle \Phi \rangle$; for vector representations it will be matrix multiplication, while for matrix representations it will be conjugation.) By considering transformations $\mu(\mathbf{x})$ which go to the identity at spatial infinity, μ defines a map $\mu : S^3 \rightarrow G$, and hence an element of $\pi_3(G)$. Elements of $\pi_3(G/H)$ are related to those of $\pi_3(G)$ by the exact homotopy sequence

$$\pi_3(G) \xrightarrow{\beta} \pi_3(G/H) \xrightarrow{\gamma} \pi_2(H) . \quad (2.3)$$

Since $\pi_2(H) = 0$ for any H , exactness implies that every element of $\pi_3(G/H)$ is the image under β of some element of $\pi_3(G)$. To construct a configuration with winding number one in the vacuum manifold, it is therefore necessary to find a map μ with an appropriate winding number in $\pi_3(G)$.

The map μ can always be written as a composition,

$$\mu = \alpha \circ \tilde{\mu} , \quad (2.4)$$

where $\tilde{\mu}$ is a fixed map from S^3 to $SU(2)$ and α maps $SU(2)$ to G . If we choose $\tilde{\mu}$ to have winding number one, then μ will represent the same winding number as α . For $\tilde{\mu} : S^3 \rightarrow SU(2)$ we choose

$$\tilde{\mu}(\mathbf{x}) = \begin{pmatrix} c_\chi + i\hat{z}s_\chi & (i\hat{x} + \hat{y})s_\chi \\ (i\hat{x} - \hat{y})s_\chi & c_\chi - i\hat{z}s_\chi \end{pmatrix} . \quad (2.5)$$

Here we have introduced the notation $c_\chi = \cos(\chi)$, $s_\chi = \sin(\chi)$, $\chi(r)$ a function of $r = \sqrt{x^2 + y^2 + z^2}$ with $\chi(0) = 0$ and $\chi(\infty) = \pi$, and $\hat{\mathbf{x}} = \mathbf{x}/r$. Construction of an appropriate field configuration then comes down to choosing the map $\alpha : SU(2) \rightarrow G$.

We begin with a theory in which $SO(4)$ breaks down to $SO(3)$. In this theory the vacuum manifold is $SO(4)/SO(3) = S^3$; it is the simplest theory containing textures, and may be thought of as the standard against which other models should be compared. The field content consists of four real scalars Φ^a ($a = 1, \dots, 4$), transforming under a vector representation of $SO(4)$. The action of an $SO(4)$ matrix O^a_b is thus $\Phi^a \mapsto O^a_b \Phi^b$. The potential is given by

$$V(\Phi^a) = \lambda(\Phi^a \Phi^a - v^2)^2 . \quad (2.6)$$

This potential is minimized when the fields attain a vev of the form

$$\langle \Phi \rangle = \begin{pmatrix} v \\ 0 \\ 0 \\ 0 \end{pmatrix} , \quad (2.7)$$

breaking $\text{SO}(4)$ to an $\text{SO}(3)$ subgroup, namely the subgroup consisting of 4×4 matrices with a one in the upper left corner, zeroes in the rest of the first row and column, and $\text{SO}(3)$ matrices in the lower right 3×3 subblock. The map α must now be a homomorphism from $\text{SU}(2)$ to $\text{SO}(4)$ with winding number one. [In fact $\pi_3(\text{SO}(4)) = \mathbf{Z} \oplus \mathbf{Z}$, so the concept of winding number is not uniquely defined. The map we choose is that which induces the generator of $\pi_3(\text{SO}(4)/\text{SO}(3))$.] If we write a general element of $\text{SU}(2)$ in terms of four real parameters e_a with $\Sigma e_a e_a = 1$,

$$g = \begin{pmatrix} e_0 + ie_3 & e_2 + ie_1 \\ -e_2 + ie_1 & e_0 - ie_3 \end{pmatrix}, \quad (2.8)$$

then an appropriate map is given by

$$\alpha(g) = \begin{pmatrix} e_0 & e_3 & e_2 & e_1 \\ -e_3 & e_0 & -e_1 & e_2 \\ -e_2 & e_1 & e_0 & -e_3 \\ -e_1 & -e_2 & e_3 & e_0 \end{pmatrix}. \quad (2.9)$$

We may think of α as replacing complex entries by real 2×2 matrices:

$$a + ib \mapsto \begin{pmatrix} a & b \\ -b & a \end{pmatrix}. \quad (2.10)$$

The composition of α with $\tilde{\mu}(\mathbf{x})$ results in a map $\mu(\mathbf{x})$ given by

$$\mu(\mathbf{x}) = \begin{pmatrix} c_\chi & \hat{z}s_\chi & \hat{y}s_\chi & \hat{x}s_\chi \\ -\hat{z}s_\chi & c_\chi & -\hat{x}s_\chi & \hat{y}s_\chi \\ -\hat{y}s_\chi & \hat{x}s_\chi & c_\chi & -\hat{z}s_\chi \\ -\hat{x}s_\chi & -\hat{y}s_\chi & \hat{z}s_\chi & c_\chi \end{pmatrix}, \quad (2.11)$$

which leads in turn to a field configuration

$$\Phi(\mathbf{x}) = v \begin{pmatrix} c_\chi \\ -\hat{z}s_\chi \\ -\hat{y}s_\chi \\ -\hat{x}s_\chi \end{pmatrix}. \quad (2.12)$$

The model in which $\text{SO}(5)$ breaks down to $\text{SO}(4)$ is closely related to the previous one. The fields are arranged into a five-vector Φ^a , with potential as in (2.6). The vacuum manifold is $\text{SO}(5)/\text{SO}(4) = S^4$, for which $\pi_3(S^4) = 0$; there are therefore no configurations

with nonzero winding number. Nevertheless, we can set up configurations which look just like those in the previous theory and see how they evolve. This serves as a test of the importance of the topology of the vacuum manifold in texture scenarios.

The configurations we consider are maps from S^3 to S^4 which lie at a constant distance from the north pole in S^4 . They are given by

$$\Phi(\mathbf{x}) = v \begin{pmatrix} ac_\chi \\ -a\hat{z}s_\chi \\ -a\hat{y}s_\chi \\ -a\hat{x}s_\chi \\ \sqrt{1-a^2} \end{pmatrix}. \quad (2.13)$$

The parameter a determines the distance from the north pole; $a = 1$ corresponds to the equator of S^4 , while $a = 0$ puts the entire field configuration at the pole (a single point).

Another closely related theory features $\text{SO}(5)$ breaking down to $\text{SO}(3)$. This model provides an interesting comparison with $\text{SO}(4)/\text{SO}(3)$, since in this case $\pi_3(G/H)$ is the finite group \mathbf{Z}_2 . There are ten real scalar fields, arranged into two five-vectors Φ_1^a and Φ_2^a , with potential

$$V(\Phi_1^a, \Phi_2^b) = \lambda_1 (\Phi_1^a \Phi_1^a - v_1^2)^2 + \lambda_2 (\Phi_2^b \Phi_2^b - v_2^2)^2 + \eta (\Phi_1^a \Phi_2^a)^2. \quad (2.14)$$

The fields acquire vevs of the form

$$\langle \Phi_1 \rangle = \begin{pmatrix} v_1 \\ 0 \\ 0 \\ 0 \\ 0 \end{pmatrix}, \quad \langle \Phi_2 \rangle = \begin{pmatrix} 0 \\ v_2 \\ 0 \\ 0 \\ 0 \end{pmatrix}. \quad (2.15)$$

We act on these fields by a 5×5 matrix with (2.11) as the upper left 4×4 subblock, a one in the lower right corner, and zeroes elsewhere. (Note that a single $\text{SO}(5)$ matrix acts simultaneously on the two vectors.) The resulting configuration is

$$\Phi_1 = v_1 \begin{pmatrix} c_\chi \\ -\hat{z}s_\chi \\ -\hat{y}s_\chi \\ -\hat{x}s_\chi \\ 0 \end{pmatrix}, \quad \Phi_2 = v_2 \begin{pmatrix} \hat{z}s_\chi \\ c_\chi \\ \hat{x}s_\chi \\ -\hat{y}s_\chi \\ 0 \end{pmatrix}. \quad (2.16)$$

We next consider a theory where $SU(3)$ is completely broken ($H = 0$). (The appearance of textures in a particle physics model with this symmetry-breaking pattern was examined in [9].) The lower homotopy groups of the resulting vacuum manifold are the same as those of $SO(4)/SO(3)$, although the number of fields and the dimensionality of the vacuum manifold are both greater. The fields consist of two complex three-vectors Φ_1^a and Φ_2^a , for a total of twelve real degrees of freedom. The potential is given by

$$V(\Phi_1^a, \Phi_2^b) = \lambda_1 \left(\Phi_1^\dagger \Phi_1 - v_1^2 \right)^2 + \lambda_2 \left(\Phi_2^\dagger \Phi_2 - v_2^2 \right)^2 + \eta \left(\Phi_1^\dagger \Phi_2 + \Phi_2^\dagger \Phi_1 \right)^2. \quad (2.17)$$

The fields attain vacuum expectation values of

$$\langle \Phi_1 \rangle = \begin{pmatrix} v_1 \\ 0 \\ 0 \end{pmatrix}, \quad \langle \Phi_2 \rangle = \begin{pmatrix} 0 \\ v_2 \\ 0 \end{pmatrix}. \quad (2.18)$$

In this case the map $\alpha : SU(2) \rightarrow SU(3)$ is simply inclusion of a 2×2 matrix into the upper left corner of a 3×3 matrix. Performing the transformation $\mu = \alpha \circ \tilde{\mu}$ on the two vectors then yields

$$\Phi_1 = v_1 \begin{pmatrix} c_\chi + i\hat{z}s_\chi \\ (i\hat{x} - \hat{y})s_\chi \\ 0 \end{pmatrix}, \quad \Phi_2 = v_2 \begin{pmatrix} (i\hat{x} + \hat{y})s_\chi \\ c_\chi - i\hat{z}s_\chi \\ 0 \end{pmatrix}. \quad (2.19)$$

The theory in which $SO(3)$ breaks down to $SO(2)$ is once again similar to $SO(4)$ breaking to $SO(3)$. The resulting textures are known as ‘‘Hopf textures’’ [10]. The fields comprise a real three-vector Φ^a with potential of the form (2.6), which leads to a vev

$$\langle \Phi \rangle = \begin{pmatrix} v \\ 0 \\ 0 \end{pmatrix}. \quad (2.20)$$

The vacuum manifold is $SO(3)/SO(2) = S^2$, for which both π_2 and π_3 are \mathbf{Z} . The theory therefore contains monopoles as well as textures. Unlike the two cases above the map α of (2.9) will clearly not suffice. Instead with g as in (2.8), we set

$$\alpha(g) = \begin{pmatrix} e_0^2 + e_1^2 - e_2^2 - e_3^2 & 2(e_1e_2 + e_0e_3) & 2(e_1e_3 - e_0e_2) \\ 2(e_1e_2 - e_0e_3) & e_0^2 - e_1^2 + e_2^2 - e_3^2 & 2(e_2e_3 + e_0e_1) \\ 2(e_1e_3 + e_0e_2) & 2(e_2e_3 - e_0e_1) & e_0^2 - e_1^2 - e_2^2 + e_3^2 \end{pmatrix}. \quad (2.21)$$

This map is the standard double cover of $\text{SO}(3)$ by $\text{SU}(2)$. (The winding number is nevertheless one; there are no single covers.) Its composition with $\tilde{\mu}(\mathbf{x})$ from (2.5) results in

$$\mu = \begin{pmatrix} c_\chi^2 + (2\hat{x}^2 - 1)s_\chi^2 & 2(\hat{x}\hat{y}s_\chi^2 - \hat{z}c_\chi s_\chi) & 2(\hat{x}\hat{z}s_\chi^2 + \hat{y}c_\chi s_\chi) \\ 2(\hat{x}\hat{y}s_\chi^2 + \hat{z}c_\chi s_\chi) & c_\chi^2 + (2\hat{y}^2 - 1)s_\chi^2 & 2(\hat{y}\hat{z}s_\chi^2 - \hat{x}c_\chi s_\chi) \\ 2(\hat{x}\hat{z}s_\chi^2 - \hat{y}c_\chi s_\chi) & 2(\hat{y}\hat{z}s_\chi^2 + \hat{x}c_\chi s_\chi) & c_\chi^2 + (2\hat{z}^2 - 1)s_\chi^2 \end{pmatrix}. \quad (2.22)$$

The resulting field configuration is straightforward:

$$\Phi(\mathbf{x}) = v \begin{pmatrix} c_\chi^2 + (2\hat{x}^2 - 1)s_\chi^2 \\ 2(\hat{x}\hat{y}s_\chi^2 + \hat{z}c_\chi s_\chi) \\ 2(\hat{x}\hat{z}s_\chi^2 - \hat{y}c_\chi s_\chi) \end{pmatrix}. \quad (2.23)$$

Adding an additional three-vector to the above theory yields a model in which $\text{SO}(3)$ is completely broken. The vacuum manifold is therefore $\text{SO}(3)$ itself, which supports \mathbf{Z}_2 strings as well as textures. The potential is of the form (2.14), leading to vevs of the form

$$\langle \Phi_1 \rangle = \begin{pmatrix} v_1 \\ 0 \\ 0 \end{pmatrix}, \quad \langle \Phi_2 \rangle = \begin{pmatrix} 0 \\ v_2 \\ 0 \end{pmatrix}. \quad (2.24)$$

Acting on these fields with (2.22) gives the following field configuration:

$$\Phi_1(\mathbf{x}) = v_1 \begin{pmatrix} c_\chi^2 + (2\hat{x}^2 - 1)s_\chi^2 \\ 2(\hat{x}\hat{y}s_\chi^2 + \hat{z}c_\chi s_\chi) \\ 2(\hat{x}\hat{z}s_\chi^2 - \hat{y}c_\chi s_\chi) \end{pmatrix}, \quad \Phi_2(\mathbf{x}) = v_2 \begin{pmatrix} 2(\hat{x}\hat{y}s_\chi^2 - \hat{z}c_\chi s_\chi) \\ c_\chi^2 + (2\hat{y}^2 - 1)s_\chi^2 \\ 2(\hat{y}\hat{z}s_\chi^2 + \hat{x}c_\chi s_\chi) \end{pmatrix}. \quad (2.25)$$

We turn now to a model in which an $\text{SO}(4)$ symmetry is broken to $\text{U}(2)$. This is accomplished by a set of six scalars which transform in the antisymmetric tensor representation of $\text{SO}(4)$, $\Phi^{ab} = -\Phi^{ba}$. The action of an $\text{SO}(4)$ transformation O on the fields is given by $\Phi \mapsto O^T \Phi O$. The quartic potential invariant under this symmetry is given by

$$V(\Phi^{ab}) = -\frac{1}{2}m^2 \text{Tr}(\Phi^T \Phi) + \frac{1}{4}\lambda_1 [\text{Tr}(\Phi^2)]^2 + \frac{1}{4}\lambda_2 \text{Tr}(\Phi^4), \quad (2.26)$$

where Φ^n refers to matrix multiplication. The fields acquire a vev of the form

$$\langle \Phi \rangle = v \begin{pmatrix} 0 & 1 & 0 & 0 \\ -1 & 0 & 0 & 0 \\ 0 & 0 & 0 & 1 \\ 0 & 0 & -1 & 0 \end{pmatrix}. \quad (2.27)$$

In this case we cannot use (2.11) to act on the vev, since this transformation is actually in the unbroken subgroup $H = \text{U}(2)$, and hence leaves (2.27) invariant. (The generator of $\pi_3(\text{SO}(4)/\text{U}(2))$ and the generator of $\pi_3(\text{SO}(4)/\text{SO}(3))$ are inherited from the two different generators of $\pi_3(\text{SO}(4)) = \mathbf{Z} \oplus \mathbf{Z}$.) Instead we take the $\text{SO}(3)$ transformation (2.22) and include it in $\text{SO}(4)$ by putting a one in the lower right corner and zeroes elsewhere. Acting the result on (2.27) yields a field configuration

$$\Phi = v \begin{pmatrix} 0 & c_\chi^2 + (2\hat{z}^2 - 1)s_\chi^2 & -2(\hat{x}c_\chi s_\chi + \hat{y}\hat{z}s_\chi^2) & 2(\hat{x}\hat{z}s_\chi^2 - \hat{y}c_\chi s_\chi) \\ -c_\chi^2 - (2\hat{z}^2 - 1)s_\chi^2 & 0 & 2(\hat{x}\hat{z}s_\chi^2 - \hat{y}c_\chi s_\chi) & 2(\hat{y}\hat{z}s_\chi^2 + \hat{x}c_\chi s_\chi) \\ 2(\hat{x}c_\chi s_\chi + \hat{y}\hat{z}s_\chi^2) & -2(\hat{x}\hat{z}s_\chi^2 - \hat{y}c_\chi s_\chi) & 0 & c_\chi^2 + (2\hat{z}^2 - 1)s_\chi^2 \\ -2(\hat{x}\hat{z}s_\chi^2 - \hat{y}c_\chi s_\chi) & -2(\hat{y}\hat{z}s_\chi^2 + \hat{x}c_\chi s_\chi) & -c_\chi^2 - (2\hat{z}^2 - 1)s_\chi^2 & 0 \end{pmatrix}. \quad (2.28)$$

Our final model features $\text{SO}(5)$ breaking down to $\text{SO}(3) \times \text{SO}(2) \times \mathbf{Z}_2$. There are fourteen scalar fields transforming in the symmetric and traceless tensor representation of $\text{SO}(5)$: $\Phi^{ab} = \Phi^{ba}$, $\text{Tr} \Phi = 0$. The potential is

$$V(\Phi^{ab}) = -\frac{1}{2}m^2 \text{Tr}(\Phi^2) + \frac{1}{4}\lambda_1[\text{Tr}(\Phi^2)]^2 + \frac{1}{4}\lambda_2 \text{Tr}(\Phi^4), \quad (2.29)$$

leading to a vev of the form

$$\langle \Phi \rangle = v \begin{pmatrix} 2 & 0 & 0 & 0 & 0 \\ 0 & 2 & 0 & 0 & 0 \\ 0 & 0 & 2 & 0 & 0 \\ 0 & 0 & 0 & -3 & 0 \\ 0 & 0 & 0 & 0 & -3 \end{pmatrix}. \quad (2.30)$$

The map $\mu(\mathbf{x})$ we have already found in (2.11). Its action on the vev yields the field configuration $\Phi = \mu^T \langle \Phi \rangle \mu$, which in components is

$$\Phi = v \begin{pmatrix} 2 - 5\hat{x}^2 s_\chi^2 & -5\hat{x}\hat{y}s_\chi^2 & 5\hat{x}\hat{z}s_\chi^2 & 5\hat{x}c_\chi s_\chi & 0 \\ -5\hat{x}\hat{y}s_\chi^2 & 2 - 5\hat{y}^2 s_\chi^2 & 5\hat{y}\hat{z}s_\chi^2 & 5\hat{y}c_\chi s_\chi & 0 \\ 5\hat{x}\hat{z}s_\chi^2 & 5\hat{y}\hat{z}s_\chi^2 & 2 - 5\hat{z}^2 s_\chi^2 & -5\hat{z}c_\chi s_\chi & 0 \\ 5\hat{x}c_\chi s_\chi & 5\hat{y}c_\chi s_\chi & -5\hat{z}c_\chi s_\chi & 2 - 5c_\chi^2 & 0 \\ 0 & 0 & 0 & 0 & -3 \end{pmatrix}. \quad (2.31)$$

To compare the different theories, we would like to compare the evolution of configurations which are in some sense “the same,” despite being in different models. For example,

it would be reasonable to compare the collapse of initially spherically symmetric textures. In all of the above field configurations, the initial energy density is spherically symmetric if we choose the radial function

$$\chi(r) = 2 \arctan(r) . \quad (2.32)$$

Indeed, with this choice the energy density profiles are identical (up to an overall normalization); they are given by

$$\rho(x, y, z) \propto \frac{1}{(1 + r^2)^2} . \quad (2.33)$$

In this sense, the initial configurations we consider are directly comparable.

However, there is a more restrictive definition of spherical symmetry: that a configuration which is rotated about the origin in space can always be brought to its original form by a global symmetry transformation. Not all of the theories we consider allow configurations which are symmetric in this strict sense. It is straightforward to check, by considering infinitesimal spatial rotations and transformations in the symmetry group G , that all of the textures in the models without defects [$\text{SO}(4)/\text{SO}(3)$, $\text{SO}(5)/\text{SO}(4)$, $\text{SO}(5)/\text{SO}(3)$, and $\text{SU}(3)/0$] are spherically symmetric, and in addition the configuration in $\text{SO}(5)/[\text{SO}(3) \times \text{SO}(2) \times \mathbf{Z}_2]$ is as well. In the remaining theories it is impossible to set up a truly spherically symmetric configuration. For the theories based on $\text{SO}(3)/\text{SO}(2) = S^2$ and $\text{SO}(4)/\text{U}(2) = \mathbf{R}P^2$, the vacuum manifolds are two-dimensional (and the map from space to the vacuum manifold is onto); therefore, the preimage of any given point in the vacuum manifold will be a one-dimensional region of space, which in general will not be taken into another such one-dimensional preimage under a spatial rotation. In the $\text{SO}(3)/0 = \mathbf{R}P^3$ theory, meanwhile, the spatial rotation has precisely two fixed points (the origin and the point at infinity), while the group action has none; therefore, a rotation cannot be undone by a group transformation.

As we shall see, this lack of true spherical symmetry will manifest itself in our simulations. This can be traced to the following effect: if a configuration is not truly symmetric

but has a symmetric energy density, deformations of the configuration along different coordinate axes will not yield configurations of equal energy. Hence, there will be an instability to non-spherical collapse. We will see this explicitly in our simulations of textures with initially spherically symmetric energy densities. Furthermore, we also perform simulations of oblate and prolate textures, obtained from those with symmetric energy densities by deforming along one axis. For the truly symmetric initial configurations, the axis chosen is of no consequence, and the energy density of the deformed texture is simply the deformed energy density of the symmetric texture. The configurations which are not truly symmetric, however, have a preferred direction [the x -axis for (2.23), and the z -axis for (2.25) and (2.28), with our conventions]. A deformation orthogonal to the preferred direction results in a triaxial energy density with no rotational symmetry, while a deformation along the preferred direction yields an axially symmetric energy density. In $\text{SO}(3)/0$ this axially symmetric pattern is very similar to that of the models which allow spherical symmetry, while in $\text{SO}(3)/\text{SO}(2)$ and $\text{SO}(4)/\text{U}(2)$ the resulting energy density is toroidal. In Figure One we have plotted the energy densities in two-dimensional slices through two representative deformed configurations, $\text{SO}(4)/\text{SO}(3)$ and $\text{SO}(3)/\text{SO}(2)$.

The energy density profiles of the oblate and prolate configurations are therefore not identical in different theories, and consequently the comparison between the models is not as direct as in the initially symmetric case. We will see below, however, that the difference is not crucial. For our simulations of deformed textures, we have always performed the deformation along the preferred axis, so that the comparison is always between configurations with axially symmetric energy densities.

III. Numerical Implementation

We integrate the field equations of motion using a standard staggered leapfrog algorithm, using a method that is second-order in time but which uses fourth-order spatial differences (as in [8], except we have added fourth-order spatial differences for better res-

olution). The field equations for the above Lagrangian with a general potential $V(\Phi)$ are

$$\frac{\partial^2}{\partial t^2}\Phi - \nabla^2\Phi + \frac{\partial V}{\partial\Phi} = 0 . \quad (3.1)$$

Here, the field Φ is vector or tensor valued, depending on which theory we are integrating. In the staggered leapfrog method, the momenta of the field $\pi = \dot{\Phi}$ are defined on half-integer timesteps. Using finite differences as an approximation to the differential operators, the expression for the field at discrete timestep $n + 1$ and Cartesian grid location $x = i\Delta x$, $y = j\Delta x$ and $z = k\Delta x$ is

$$\Phi_{ijk}^{n+1} = \Delta t \pi_{ijk}^{n+1/2} + \Phi_{ijk}^n \quad (3.2)$$

and from the field equations, combined with the momentum definition, we obtain the expression

$$\begin{aligned} \pi_{ijk}^{n+1/2} = \pi_{ijk}^{n-1/2} - \frac{\Delta t}{\Delta x^2} & (\Phi_{i+2,jk}^n + \Phi_{i,j+2,k}^n + \Phi_{ij,k+2}^n - 16\Phi_{i+1,jk}^n - 16\Phi_{i,j+1,k}^n \\ & - 16\Phi_{ij,k+1}^n + 90\Phi_{ijk}^n - 16\Phi_{i-1,jk}^n - 16\Phi_{i,j-1,k}^n \\ & - 16\Phi_{ij,k-1}^n + \Phi_{i-2,jk}^n + \Phi_{i,j-2,k}^n + \Phi_{ij,k-2}^n) - \Delta t \frac{\partial V}{\partial\Phi} \end{aligned} \quad (3.3)$$

for π at timestep $n + 1/2$.

We use Neumann boundary conditions. In our simulations, once the initial texture configuration collapses, massless and massive radiation hits the wall, then some of it is reflected and influences the subsequent evolution of the field inside the box. In our production simulations, we take the radius of the texture to be 10 gridzones, while the simulation volume is $64 \times 64 \times 64$ gridzones. With this geometry, reflected radiation does not influence the texture configuration until after it has collapsed and the decay products (either defects or radiation) have had time to propagate away from the texture core to a distance of order the initial size.

The initial texture configurations are discussed above for the various theories which we have simulated. For the purposes of the numerical simulation it is convenient to have an

initial condition with zero energy at the boundaries of the simulation volume; we therefore modify the radial function $\chi(r)$ given in (3.32) so that the fields are initially constant outside a fixed radius:

$$\chi(r) = \begin{cases} 2 [1 - e^{\beta(r-R)}] \arctan(r) & \text{for } r \leq R , \\ \pi & \text{for } r > R , \end{cases} \quad (3.4)$$

with β and R set such that χ goes smoothly to π at the finite radius R . We also examined textures in a theory where $SU(3)$ was spontaneously broken to $SO(3)$; in this model, however, no natural choice of $\chi(r)$ led to a symmetric energy density. We have therefore not included this model in our comparisons.

There are two conditions on the timestep for a global symmetry breaking theory. One is the usual Courant condition $\sqrt{2}\Delta t \leq \Delta x$. In addition, the source term from the derivative of the potential $\partial V/\partial\Phi$ adds an effective mass term to the equations. For stability, the timestep must be short enough that variations in the field are well resolved. One way to see this is to look at a vector theory in the situation where the field is spatially constant. We then have an equation

$$\ddot{\Phi} = -\lambda(|\Phi|^2 - v^2)\Phi , \quad (3.5)$$

where the effective mass is $\lambda(|\Phi|^2 - v^2)$. If we normalize v to be 1, then when Φ is close to zero and at the core of the potential, the effective mass is at a maximum, and the solution to the above differential equation has a wavenumber of $\lambda^{1/2}$. To resolve the solution for this wavenumber, we typically take the timestep to be 1/10 of the wavelength.

For the parameters of the scalar potential, we take the quartic self-coupling of the field to be $\lambda = 0.1$, and the magnitude of the vacuum expectation value to be $v = 0.1$. The $SO(5)/SO(4)$ model contains the additional parameter a , which characterizes where on the vacuum manifold S^4 the initial configuration lies; we have used $a = 0.1$ in the simulations shown. (Additional simulations with other values of a led to indistinguishable

results.) Together with a timestep $\Delta t \simeq 0.1$ our code is stable for all collapses in the theories studied.

To ensure stability and the accuracy of the code, we check that the total energy within the simulation volume is constant. We find that for the above parameters, the energy is typically constant to within 1%. There is often a slight increase due to the production of massive radiation. This is due to an increase in the effective mass of the field, and subsequently a poorer resolution of fluctuations in the field (discussed above) in time.

IV. Results

For each of the eight models listed in Table One, we performed three simulations of single-texture collapse; one with a spherically symmetric initial configuration, one with an oblate initial configuration, and one with a prolate initial configuration. The oblate and prolate configurations were obtained by scaling the configuration along either one or two axes by a factor of 0.5. At each timestep in the simulations we calculate the total energy E , as well as the separate values of the kinetic energy E_k , gradient energy E_g , and potential energy E_V :

$$\begin{aligned}
 E &= E_k + E_g + E_V \\
 E_k &= \int d^3x \left(\frac{\partial \Phi}{\partial t} \right)^2 \\
 E_g &= \int d^3x (\nabla \Phi)^2 \\
 E_V &= \int d^3x V(\Phi) .
 \end{aligned} \tag{4.1}$$

To measure the asymmetries in the collapse, we computed the quadrupole moments of the total energy in a sphere of radius the initial texture size:

$$Q_{ij} = \int_{r < R} d^3x (3x^i x^j - \delta^{ij} r^2) \rho(\mathbf{x}), \tag{4.2}$$

where ρ is the total energy density. Since we set up our configurations with initial asymmetries along the coordinate axes, we are interested in the moments Q_{ii} which measure the asymmetry along the x^i axis.

We examine first the four models listed in Table One which do not support strings or monopoles; $\pi_1(\mathcal{M}) = \pi_2(\mathcal{M}) = 0$. In Figure Two we have plotted the integrated energies (total, gradient, kinetic and potential) for the evolution of initially symmetric configurations in each of these theories. The total energy is normalized to 100 for purposes of comparison. These graphs reveal several features which are common to all of the collapse simulations we studied. The configuration starts out with zero kinetic and potential energy. As the texture collapses the potential energy grows slightly, but remains a small part of the total energy throughout the simulation. The kinetic and gradient energies move toward equipartition, although this is not necessarily completely successful. In every simulation we performed, the graphs of the kinetic and gradient energies approach each other and cross at least once; the point where they are first equal serves as a convenient measure of the timescale for the collapse. In the simulations shown in Figure Two, equality is reached after approximately 75 timesteps.

A remarkable feature of these four graphs is their similarity with respect to each other. In the $\text{SO}(4)/\text{SO}(3)$ and $\text{SO}(5)/\text{SO}(4)$ theories the kinetic and gradient energies do not equipartition quite as effectively as in the $\text{SO}(5)/\text{SO}(3)$ and $\text{SU}(3)/0$ theories, but the difference is small. As we shall see below, the differences within this set of models are much less than the differences between them and the models which support defects (strings or monopoles).

The results of the $\text{SO}(5)/\text{SO}(4)$ simulation are especially noteworthy, since in that theory the initial configuration is topologically trivial [$\pi_3(\text{SO}(5)/\text{SO}(4)) = 0$]. Nevertheless, the evolution of the energy densities proceeds in a manner practically indistinguishable from that in $\text{SO}(4)/\text{SO}(3)$. (The fact that such configurations would collapse was noted in [2]; our simulations provide dynamical evidence that the collapse is almost identical to those in theories with nontrivial $\pi_3(\mathcal{M})$.) The only noticeable difference is in the potential energy, which remains essentially zero throughout the $\text{SO}(5)/\text{SO}(4)$ collapse, while rising

slightly in the other models. This is due to the fact that, in the theories with topologically nontrivial configurations, the fields must climb out of the vacuum manifold in order to unwind, which necessarily induces a nonzero potential energy. Since the potential energy is nevertheless only a small contributor to the total energy of the texture, these simulations indicate that the behavior characteristic of “texture collapse” may arise even without nontrivial topology. (Of course the frequency with which such behavior actually does arise in a cosmological context is not addressed by our simulations, and may be different in the different models.)

We have not shown the evolution of the quadrupole moments for these simulations, since they vanish throughout the course of the collapse. This simply indicates that these models remain spherically symmetric if they begin in a symmetric configuration.

In Figure Three we have plotted the same quantities as in Figure Two, in the same set of models, this time for initially oblate configurations. (The results for prolate collapse will not be shown, as they are essentially identical to the oblate case.) Once again, the results of these four simulations are very similar to one another. They are also similar to the results for initially symmetric configurations; again we see the equipartition of kinetic and gradient energies, while the potential energy is much smaller. The timescale for these collapses is slightly less than that in the symmetric case; the kinetic and gradient energies first become equal after approximately 60 timesteps. This difference can be traced to the fact that the initial configurations are somewhat smaller, as they are obtained from the symmetric configurations by shrinking by 50% along the x -axis.

The quadrupole moments for the evolution of the initially oblate configurations in models without strings or monopoles are shown in Figure Four. The three quantities Q_{xx} , Q_{yy} and Q_{zz} are plotted; only two curves are visible because the initial deformation is along the x -axis, and hence $Q_{yy} = Q_{zz}$ throughout the simulation. The quadrupoles begin at a certain value, head toward zero, and cross the axis before settling smoothly toward zero.

The physical interpretation is that the initially oblate configuration moves toward spherical symmetry, then overshoots to become somewhat prolate. The quadrupole moments are only calculated in a sphere of radius equal to the initial texture size, so, as the radiation leaves the sphere, the quadrupole goes to zero. The remarkable resemblance between the different simulations is the strongest evidence that texture collapse is essentially the same in these four models; not only do the total energies partition in similar ways, but the spatial distribution of the total energy density for nonspherical initial configurations also evolves similarly.

We turn next to the four models listed in Table One which support strings or monopoles. (The initial configurations that we set up are pure texture, since the fields are everywhere in the vacuum manifold, but these models allow topologically stable defect configurations.) In Figure Five we have plotted the integrated energies (total, gradient, kinetic and potential) for the collapse of configurations with initially spherically symmetric energy densities in these models. The four graphs are similar to each other, although we shall see below that these models are distinguishable by other measures. As in the models that do not support defects, the kinetic and gradient energies evolve toward equipartition, while the potential energy is always significantly smaller. A comparison between Figures Two and Five, however, reveals that there are important differences between the spherical collapses in models with and without strings or monopoles. The most significant quantifiable difference is in the timescale for collapse; in the models which allow defects, the kinetic and gradient energies become equal after only 45 timesteps, in comparison with 75 timesteps for the models of Figure Two.

Another dramatic difference is manifested in Figure Six, which shows the quadrupole moments for the collapses of initially spherical configurations in models which support defects. The notable feature of these plots is that the quadrupoles in three of the four models [$SO(3)/SO(2)$, $SO(3)/0$, and $SO(4)/U(2)$] do not vanish throughout the simula-

tion, even though the initial energy densities are spherically symmetric. As discussed at the end of Section Two, the asymmetries indicated by the nonzero quadrupoles can develop because the initial field configuration is not truly spherically symmetric, even though the energy density is. The collapse of these textures is therefore different in an important way from the collapse of truly symmetric textures, since the energy densities evolve asymmetrically. On the other hand, it is also important to recognize that in the remaining model, $\text{SO}(5)/[\text{SO}(3) \times \text{SO}(2) \times \mathbf{Z}_2]$, which is truly symmetric and does not develop a nonzero quadrupole, the partition of energy densities nevertheless resembles the other models which support defects more than those which do not. This is why it is more appropriate to classify the theories by whether or not they support strings or monopoles, rather than whether or not they admit spherically symmetric texture configurations.

Closer examination of the field values during these simulations reveals that the asymmetry leads to dramatic effects, in the form of nucleation of topological defects. Figure Seven is a three-dimensional rendering of contours of total energy density and potential energy at a single timestep during the $\text{SO}(3)/\text{SO}(2)$ simulation. This theory supports monopoles as well as textures, and the disk-shaped regions of high potential energy are monopoles and antimonopoles. A sequence of such pictures throughout the simulation reveals that the texture initially collapses in a nearly symmetric fashion. It then begins to deviate from spherical symmetry (while remaining axially symmetric), and a monopole-antimonopole pair nucleates at the center. These travel away from each other toward the edges of the simulation region, while eventually another pair nucleates at the center. The antimonopole of the second pair follows the monopole of the first, and vice-versa. Presumably these will annihilate, although the first pair leaves the box before this can occur. The simulation of $\text{SO}(4)/\text{U}(2)$ proceeds along the same lines, with identical results. This is not surprising, since the vacuum manifold $\text{SO}(4)/\text{U}(2) = \mathbf{R}P^2$ is related to the vacuum manifold $\text{SO}(3)/\text{SO}(2) = S^2$ by identification of antipodal points; the local geometry of both vacuum manifolds is therefore the same. Laboratory experiments with nematic liquid crys-

tals [11] have seen evidence of similar behavior; the vacuum manifold in that case was $\mathbf{R}P^2$, and it was found that textures tended to decay into monopole-antimonopole pairs. Meanwhile, the distinct geometry of $\text{SO}(3)/0 = \mathbf{R}P^3$ leads to dramatically different evolution; in this model there are no monopoles, but the texture collapse leads to formation of a loop of cosmic string, as shown in Figure Eight. This loop grows and intersects the edges of the simulation region, so we cannot follow its entire evolution. The $\text{SO}(5)/[\text{SO}(3) \times \text{SO}(2) \times \mathbf{Z}_2]$ theory, although admitting both strings and monopoles, collapses symmetrically, and no defects are formed.

Of course, in a cosmological context it would be very unlikely for a collapsing texture to begin in a perfectly symmetric configuration. To this extent, the instability of some theories is of less importance than the evolution of initial conditions which are noticeably asymmetric. Figure Nine presents the behavior of the integrated energies in the four models which support defects, beginning from oblate initial conditions. Again, the four plots appear similar to each other, while differing from the analogous plots in Figure Three for models without strings or monopoles. The timescale for collapse is now approximately 35 timesteps, and the equipartition of kinetic and gradient energies occurs rapidly and effectively.

Figure Ten, which plots the quadrupole moments for these collapses from oblate initial conditions, indicates that the models with defects can differ from each other as well as from the models without defects. (Although it is not evident from these plots, we have checked that defects are nucleated according to the same pattern which appeared in symmetric collapses; monopole/antimonopole pairs are produced in $\text{SO}(3)/\text{SO}(2)$ and $\text{SO}(4)/\text{U}(2)$, a string loop is produced in $\text{SO}(3)/0$, and no defects are produced in $\text{SO}(5)/[\text{SO}(3) \times \text{SO}(2) \times \mathbf{Z}_2]$.) The general pattern familiar from Figure Four, where the oblate configuration became prolate before symmetrizing, is seen here as well. The quadrupole moments in the $\text{SO}(3)/\text{SO}(2)$ and $\text{SO}(4)/\text{U}(2)$ models, whose vacuum manifolds are locally equivalent,

are indistinguishable, but these two appear different from $SO(3)/0$ and $SO(5)/[SO(3) \times SO(2) \times \mathbf{Z}_2]$, which also appear slightly different from each other. As these differences represent distinct evolutions of the spatial distribution of the total energy density, they indicate the possibility that the different models could lead to distinguishable cosmological density fluctuations.

V. Discussion

We have examined the dynamics of texture collapse in a variety of scalar field theories with spontaneously broken global symmetries. Our goal was to determine whether the geometry and topology of the vacuum manifold would affect the evolution of analogous field configurations in different models. The answer is clearly “yes”; however, the cosmological significance of the effects observed is still unclear.

We have been led to two basic results. First, the collapse of a single texture configuration depends on whether the theory under consideration admits the existence of cosmic strings or monopoles. Theories which do allow such defects have textures which collapse somewhat more rapidly, and in the process of collapse may nucleate loops of string or monopole/antimonopole pairs. Second, some theories with nontrivial $\pi_3(\mathcal{M})$ admit textures with spherically symmetric energy densities, but not texture configurations which are strictly spherically symmetric. Such configurations collapse nonspherically. These two results are related; it is the configurations without true spherical symmetry that nucleate defects during collapse. In the wide class of models considered in [5], all of the theories without monopoles or strings either allow spherically symmetric textures or do not have textures at all.

From the point of view of cosmology, texture collapse is not the only important process in a theory which admits strings or monopoles; in such models the Kibble mechanism predicts that there will be an appreciable number of defects per Hubble volume, and the gravitational perturbations produced by these defects will presumably be comparable in

importance to those produced by collapsing textures. Indeed, the results of our simulations may indicate that textures are even less important in such models than might have been naively expected. The laboratory experiments of [11], involving a condensed-matter system which admitted strings, monopoles and textures, found that textures were rarely produced in a phase transition, and when a texture configuration was introduced by hand it decayed into monopole/antimonopole pairs. Our results, in which textures with initially perfectly symmetric energy densities were seen to collapse into defects, may indicate that textures will rarely form in certain theories, with defect formation being more likely. Contrariwise, the collapse of textures may provide an additional mechanism for defect production. The importance of these effects to cosmological structure formation can only be answered by large-scale numerical simulations of the evolution of the fields as the universe expands.

For the models which are free of strings and monopoles, our results provide evidence that simulations of any specific simple model [such as $SO(4)/SO(3)$] do not miss any important physical effects. We find that the collapse of textures proceeds in essentially the same way in all such theories; to this extent, simulations in one model are relevant to other models as well. Of course, there are a number of important issues which our simulations do not address, such as the frequency and distribution of texture collapse, which could in principle be different in distinct models.

Finally, our examination of the $SO(5)/SO(4)$ model provides evidence that events resembling texture collapse can occur in the absence of nontrivial topology, as suggested in [2]. Indeed, the quantitative characteristics of the collapse in this model are indistinguishable from those in the conventional $SO(4)/SO(3)$ model. Again, the relative frequency of such events in the different models is not addressed by our simulations. More detailed studies will be necessary to understand the precise differences between cosmological models based on the theories examined here.

Acknowledgments

We would like to thank Peter Arnold, Jim Bryan, Edward Farhi, Gary Gibbons, Nick Manton, Krishna Rajagopal, Mark Trodden, Neil Turok, Alex Vilenkin, and Lawrence Yaffe for helpful conversations. This work was supported in part by the National Science Foundation under grants PHY/94-07194 and PHY/92-00687, by the U.S. Department of Energy (D.O.E.) under contract no. DE-AC02-76ER03069, and by U.K. PPARC grant GR/L21488.

References

1. N. Turok, *Phys. Rev. Lett.* **63**, 2625 (1989).
2. L. Perivolaropoulos, *Phys. Rev. D* **46**, 1858 (1992).
3. U. Pen, D.N. Spergel, and N. Turok, *Phys. Rev. D* **49**, 692 (1994).
4. L.-F. Li, *Phys. Rev D* **9**, 1723 (1974).
5. J.A. Bryan, S.M. Carroll and T. Pyne, *Phys. Rev. D* **50**, 2806 (1994), hep-ph/9312254.
6. D.N. Spergel, N. Turok, W.H. Press, and B.S. Ryden, *Phys. Rev. D* **43**, 1038 (1991); R.Y. Cen, J.P. Ostriker, D.N. Spergel, and N. Turok, *Ap. J* **393**, 42 (1992); D.P. Bennett and S.H. Rhie, *Astrophys. J.* **406**, L7 (1993), hep-ph/9207244; R. Durrer, A. Howard, and Z.-H. Zhou, *Phys. Rev. D* **49**, 681 (1994), astro-ph/9311040; J. Borrill, E.J. Copeland, A.R. Liddle, A. Stebbins, and S.Veeraraghavan, *Phys. Rev. D* **50**, 2469 (1994), astro-ph/9403005; R. Durrer and Z.-H. Zhou, *Phys. Rev. Lett.* **74**, 1701 (1995), astro-ph/9407027; N.G. Phillips and A. Kogut, *Phys. Rev. Lett.* **75**, 1264 (1995), astro-ph/9507045.
7. J. Borrill, E.J. Copeland, and A.R. Liddle, *Phys. Lett.* **B258**, 310 (1991); R.A. Leese and T. Prokopec, *Phys. Rev. D* **44**, 3749 (1991); S. Aminneborg, *Nucl. Phys.* **B388**, 521 (1992); A. Sornborger, *Phys. Rev. D* **48**, 3517 (1993), astro-ph/9303005.
8. T. Prokopec, A. Sornborger, and R.H. Brandenberger, *Phys. Rev. D* **45**, 1971 (1992).
9. M. Joyce and N. Turok, *Nucl. Phys.* **B416**, 389 (1994), hep-ph/9301287.
10. S.H. Rhie and D.P. Bennett, preprint UCRL-JC-110560 (1992); X. Luo, *Phys. Lett.* **B287**, 319 (1992).
11. I. Chuang, R. Durrer, N. Turok, and B. Yurke, *Science* **251**, 1336 (1991).

G	H	N	$\pi_1(G/H)$	$\pi_2(G/H)$	$\pi_3(G/H)$	$\dim(G/H)$
SO(4)	SO(3)	4	0	0	\mathbf{Z}	3
SO(5)	SO(4)	5	0	0	0	4
SO(5)	SO(3)	10	0	0	\mathbf{Z}_2	7
SU(3)	0	12	0	0	\mathbf{Z}	8
SO(3)	SO(2)	3	0	\mathbf{Z}	\mathbf{Z}	2
SO(3)	0	6	\mathbf{Z}_2	0	\mathbf{Z}	3
SO(4)	U(2)	6	\mathbf{Z}_2	\mathbf{Z}	\mathbf{Z}	2
SO(5)	$\text{SO}(3) \times \text{SO}(2) \times \mathbf{Z}_2$	14	\mathbf{Z}_2	\mathbf{Z}	\mathbf{Z}_2	6

Table 1: Models. We list the models considered in this paper, in which a global symmetry group G is spontaneously broken to a subgroup H . N is the number of real scalar fields; the twelve real fields in the SU(3) theory are arranged into two complex three-vectors, while the other representations are explicitly real. The lower homotopy groups π_q of the vacuum manifold G/H are listed, as well as the dimensionality of G/H (corresponding to the number of massless Goldstone bosons). The models are grouped into two classes, depending on whether the model supports strings $[\pi_1(G/H)]$ and/or monopoles $[\pi_2(G/H)]$.

Figure Captions

Figure One. These plots represent energy density contours in the x - y plane of oblate configurations in the $SO(4)/SO(3)$ and $SO(3)/SO(2)$ theories. The textures are obtained from those with spherically symmetric energy densities by shrinking the configurations by 50% along the x -axis. The energy density in the $SO(4)/SO(3)$ is simply deformed along with the coordinates, while in the $SO(3)/SO(2)$ model the maximum energy density describes a ring in the y - z plane. In these figures, the three-dimensional configuration is obtained by rotation around the x -axis.

Figure Two. The integrated energy densities during the evolution of textures with initially spherically symmetric energy densities in the four theories which do not support strings or monopoles. Each form of energy density is integrated over the volume of the simulation region; the total energy is the sum of the integrated potential, kinetic and gradient energies. The horizontal axis is measured in timesteps of the simulations.

Figure Three. The integrated energy densities during the evolution of textures with initially oblate configurations (obtained from the symmetric configurations by deforming along one axis) in the four theories which do not support strings or monopoles.

Figure Four. Quadrupole moments of the total energy density for collapse of initially oblate configurations in the four theories which do not support strings or monopoles.

Figure Five. The integrated energy densities during the evolution of textures with initially spherically symmetric energy densities in the four theories which do support either strings or monopoles. (These textures are referred to as “symmetric”, although only in $SO(5)/[SO(3) \times SO(2) \times \mathbf{Z}_2]$ is the configuration truly spherically symmetric.)

Figure Six. Quadrupole moments of the total energy density for collapse of configurations with initially symmetric energy densities in the four theories which do support either strings or monopoles. Note that nonzero quadrupoles develop for three of the four models.

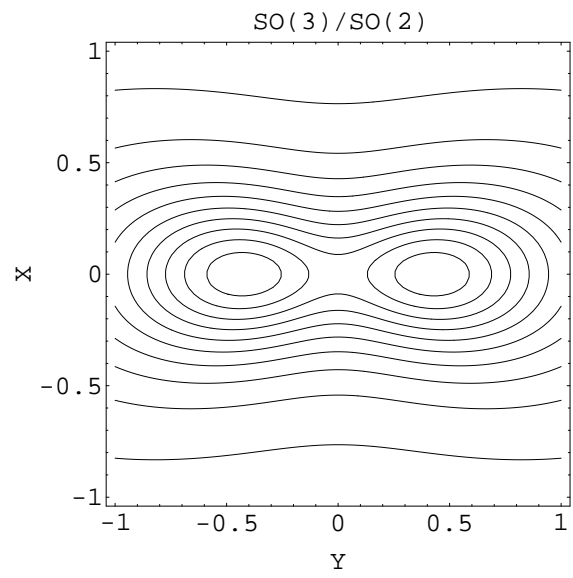
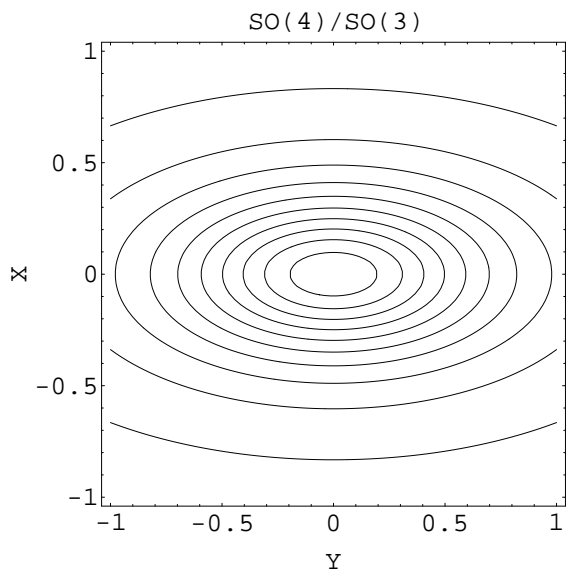
Figure Seven. Three-dimensional contours of total energy density and potential energy at one moment during the collapse of the $SO(3)/SO(2)$ configuration with an initially symmetric energy density. The shaded regions are those with large potential energies, representing monopoles and anti-monopoles. The lower total-energy contour describes a prolate spheroid, while the higher contour describes two roughly hemispherical regions associated with the inner monopole/anti-monopole pair.

Figure Eight. Three-dimensional contours of total energy density and potential energy at one moment during the collapse of the $SO(3)/0$ configuration with an initially symmetric energy density. The shaded region is one of large potential energy, representing a loop of cosmic string. The total-energy contours describe roughly spheroidal regions.

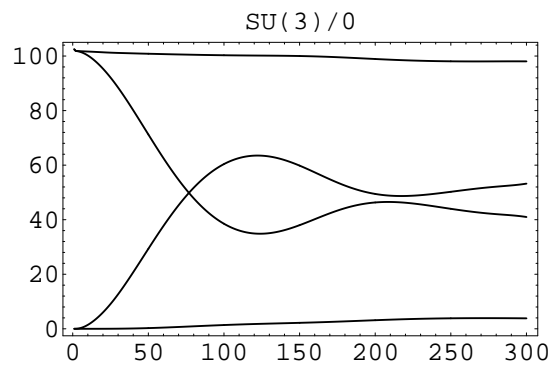
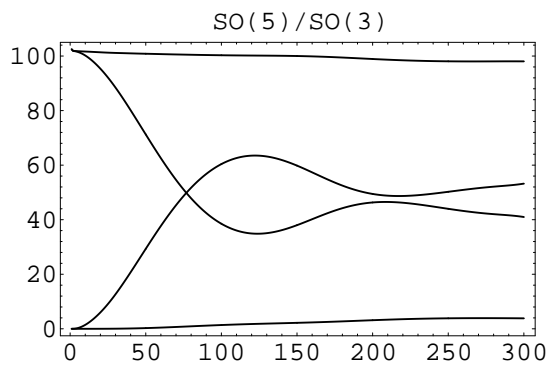
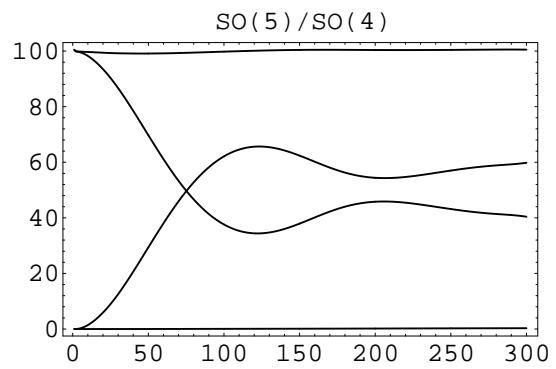
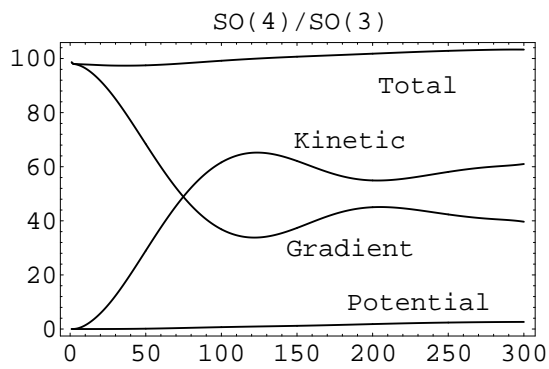
Figure Nine. The integrated energy densities during the evolution of textures with initially oblate energy densities (obtained from the symmetric configurations by deforming along one axis) in the four theories which do support either strings or monopoles.

Figure Ten. Quadrupole moments of the total energy density for collapse of initially oblate configurations in the four theories which do support either strings or monopoles.

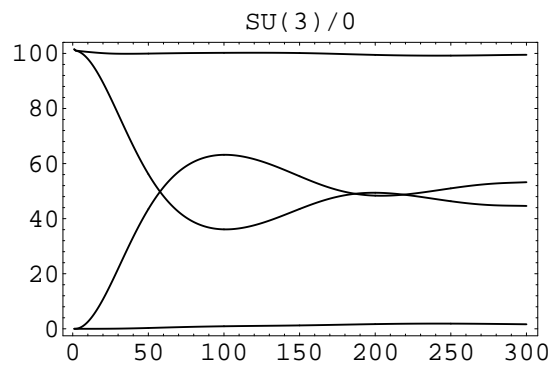
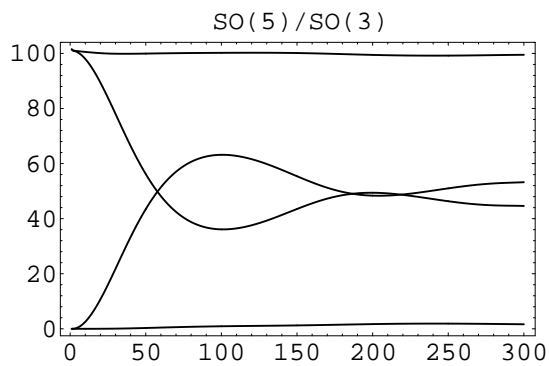
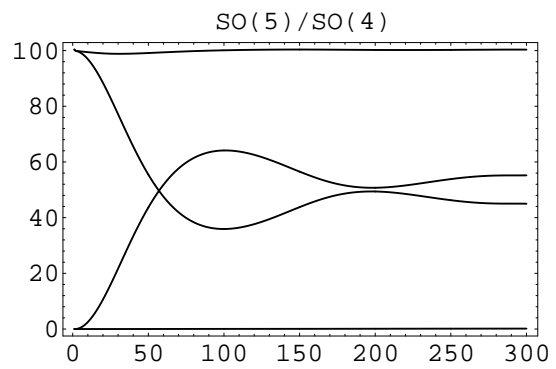
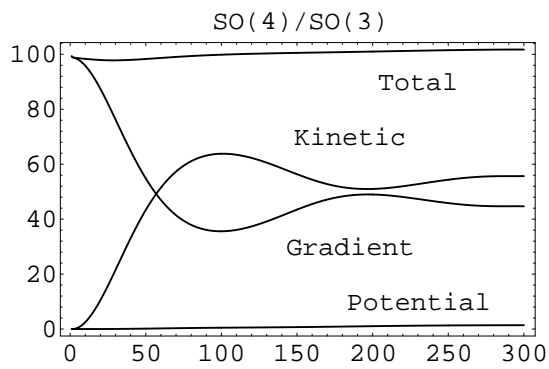
Energy Densities for Oblate Configurations



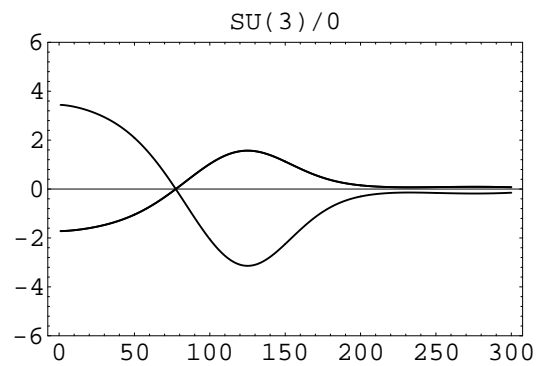
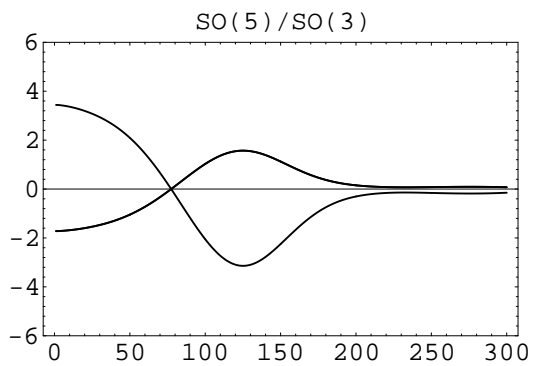
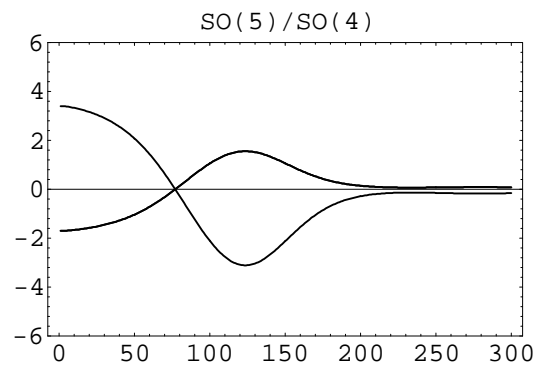
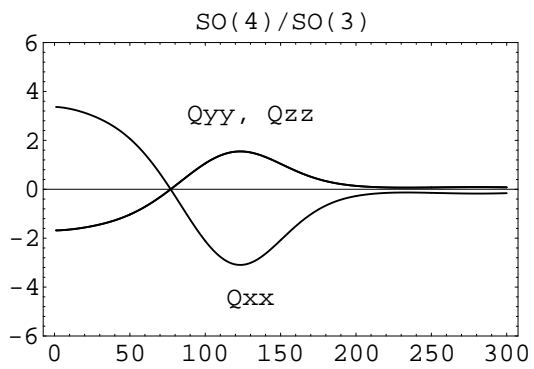
Energy evolution: Symmetric initial conditions
Theories without strings or monopoles



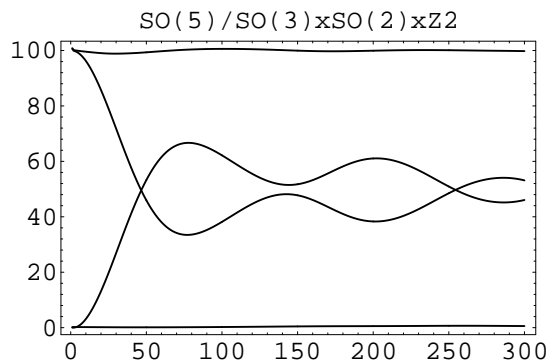
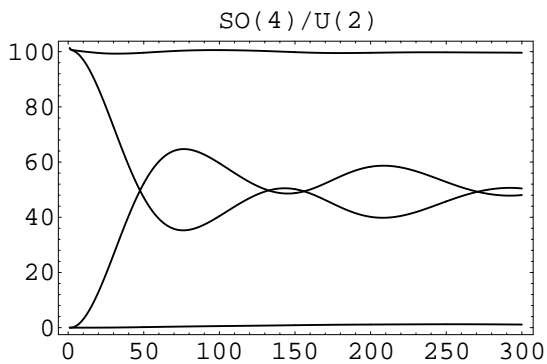
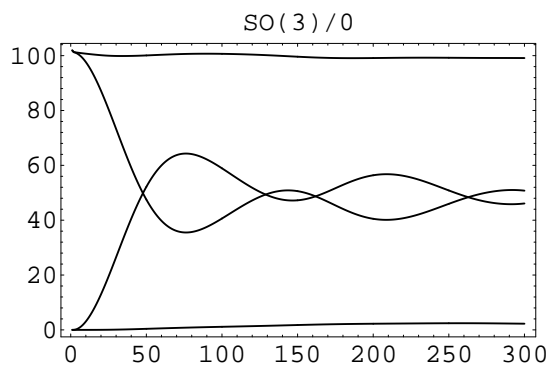
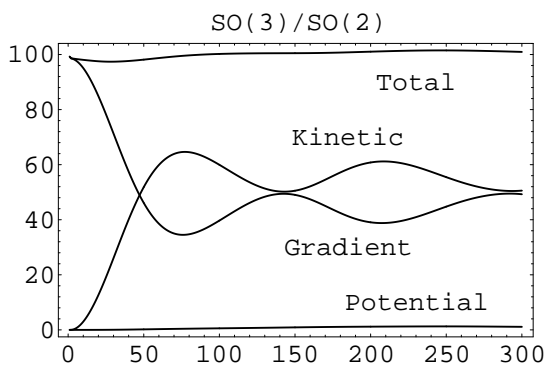
Energy evolution: Oblate initial conditions
Theories without strings or monopoles



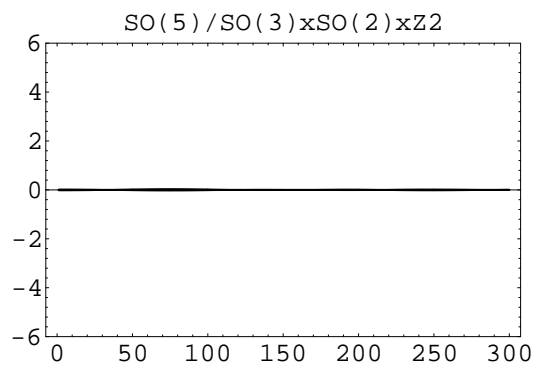
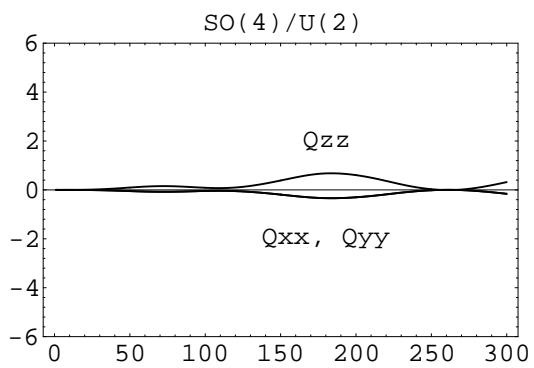
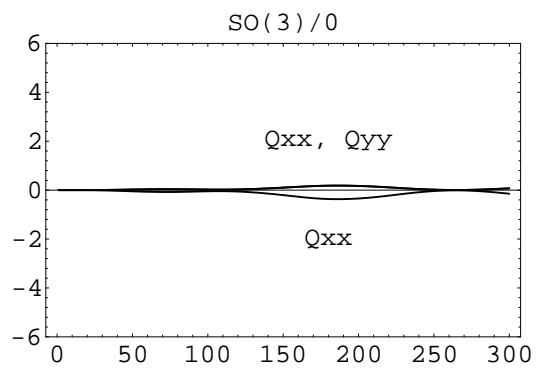
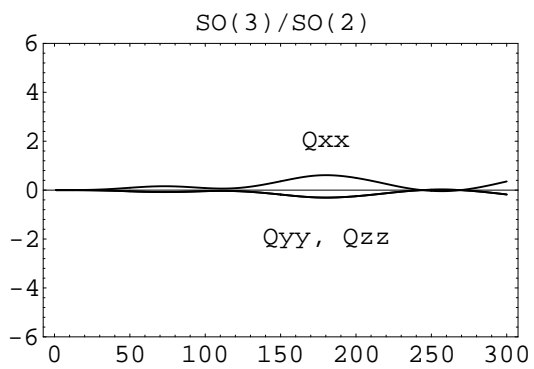
Quadrupole moments: Oblate initial conditions
Theories without strings or monopoles

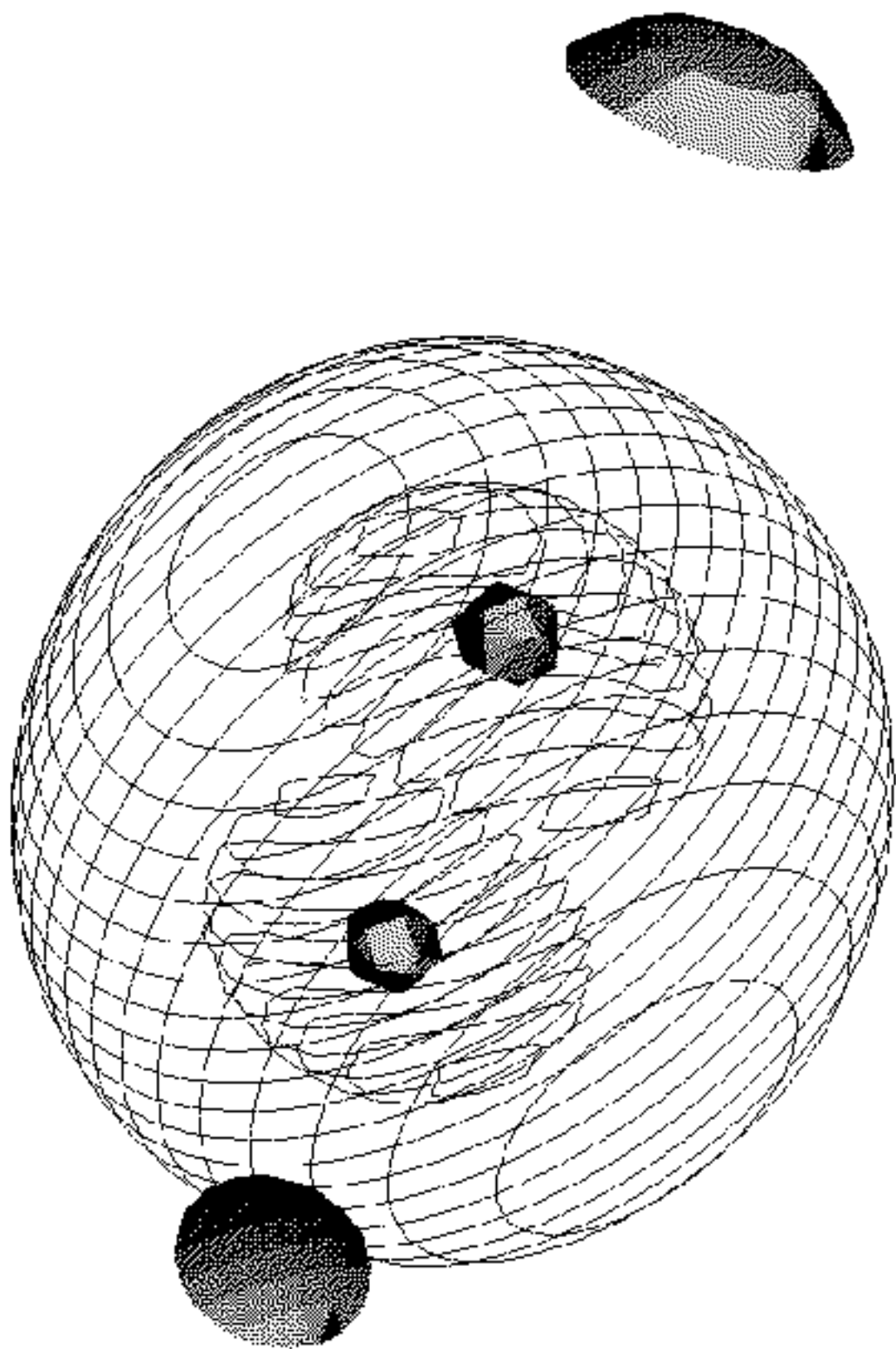


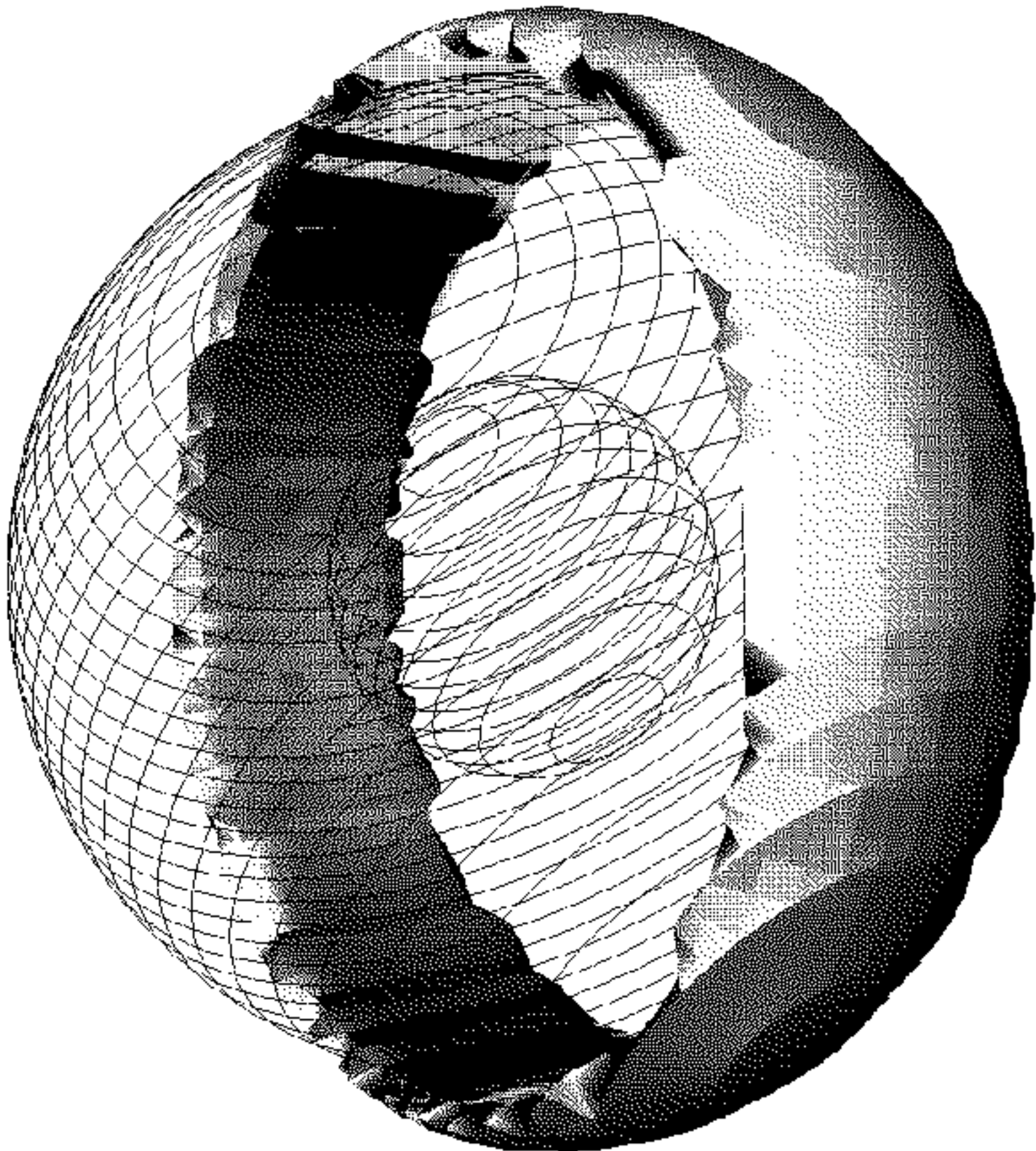
Energy evolution: Symmetric initial conditions
Theories with strings and/or monopoles



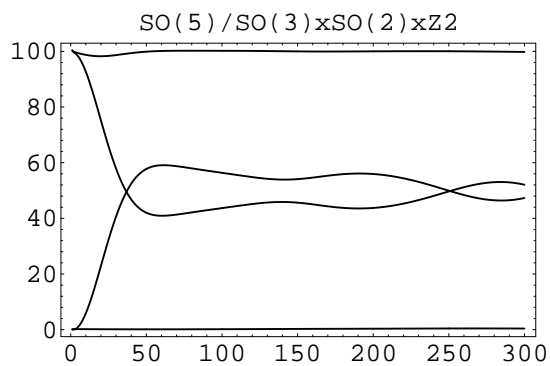
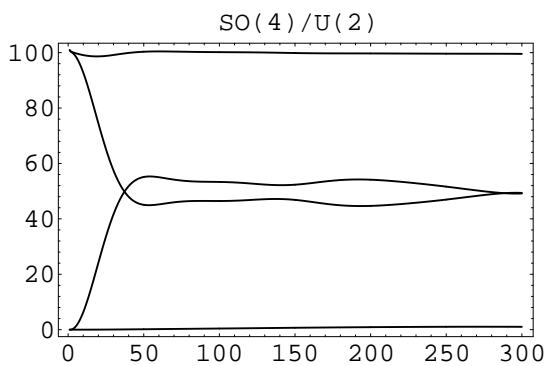
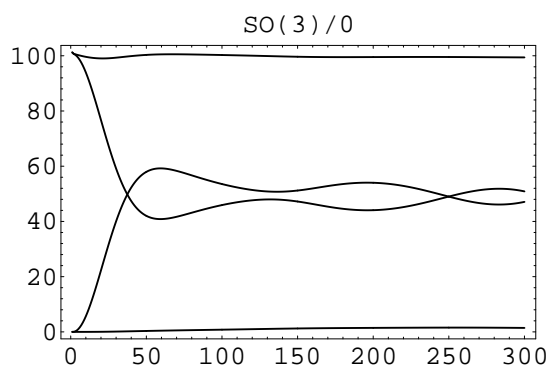
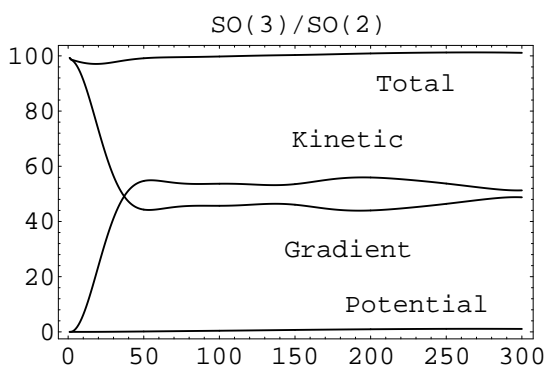
Quadrupole moments: Symmetric initial conditions
Theories with strings and/or monopoles







Energy evolution: Oblate initial conditions
Theories with strings and/or monopoles



Quadrupole moments: Oblate initial conditions
Theories with strings and/or monopoles

